

Numerical Investigation of the Influences of the Features of Transonic Flow over a Hemispherical Turret on Beam Wavefront Distortions

S. Tang, J. Li[†] and Z. Wei

School of Aeronautics, Northwestern Polytechnical University, Xi'an 710072, China

[†]Corresponding Author Email: lijieruihao@nwpu.edu.cn

(Received July 1, 2022; accepted October 16, 2022)

ABSTRACT

Complex features of transonic flow over a turret make it challenging to use passive flow control to reduce aero-optical effects. In this study, the influence of different flow features on wavefront distortions is numerically investigated through improved delayed detached eddy simulation coupled with a modified sub-grid scale. The proper orthogonal decomposition (POD) method is used to study the spatiotemporal characteristics of the flow features. The flow field changes in the wake along with the motion of the shock. Two features, namely, lateral shift (dominant in modes 1 and 2) and wall-normal fluctuation (dominant in modes 3 and 4) of the wake, are the most dominant in the flow field. All beams share the common feature of transmitting the flow field, in which a large component of optical path difference (OPD) appears at $St=0.35$, indicating the high impact of wall-normal fluctuation on the distortion of the wavefront. After the different POD modes, which contain 30% of the mode energy, are removed, all beams transmitted through different reconstructed fields show very different features for OPD. The flow features that do not exhibit higher-order modes from modes 21 to 92 affect the OPD slightly, as the OPD components in the low- St region are almost unchanged. With the removal of modes from 3 to 32, wavefront distortions are considerably reduced, particularly at $St=0.35$. The wavefront distortions are most reduced after the lower order modes from 1 to 20 are removed, as the components of OPD in the low- St region are dramatically reduced. The significant relations between OPD and the flow features reveal that controlling the dominant flow features has significant potential for reducing aero-optical effects.

Keywords: IDDES; Hemispherical turret; Transonic flow; POD; Wavefront distortion.

NOMENCLATURE

A_z	azimuthal angle	St	Strouhal number
C_p	pressure coefficient	u	velocity in the x direction
El	elevation angle	v	velocity in the y direction
D	turret diameter	VTM	Vortex Tilting Measure
M_∞	free stream Mach number	w	velocity in the z direction
n	local refractive index	α	viewing angle
OPD	Optical Path Difference	β	modified elevation angle
OPD_{Norm}	Normalized Optical Path difference	ρ	dimensionless density
POD	proper orthogonal decomposition	ρ^*	local dimensional density
n	local refractive index	ρ_∞^*	dimensional free stream density
RMS	Root Mean Square	ρ_{SL}	sea-level density

1. INTRODUCTION

The effects of aero-optics under transonic free stream conditions challenge the performance of turrets in flight. The wavefront of a beam transmitted through a complex turbulent flow field around a turret is

prone to severe distortion (Gilbert and Otten 1982). The optical path difference (OPD) will be highly affected, particularly as the beam is transmitted through the wake and shock region, according to experimental data provided by the Airborne Aero-Optics Laboratory (Jumper *et al.* 2012; De Lucca *et al.* 2013; Jumper *et al.* 2013; Porter *et al.* 2013;

Jumper *et al.* 2015, 2018). The distortion of the wavefront produced in the relatively turbulent zone, which spans the turret diameter, may eventually affect the beam, causing phenomena such as defocus, jitter, pointing errors, and changes in the distribution of light intensity (Mani *et al.* 2009; Wang *et al.* 2012).

The basic regime of the turret flow field from subsonic to supersonic is introduced in previous works (Gordeyev and Jumper 2010; Wang *et al.* 2012). The topology of transonic flow over a hemisphere was introduced by Gordeyev *et al.* (2016), and wavefront distortion under transonic conditions was introduced by Morrida *et al.* (2016). Due to the presence of shock and shock-related separation at the surface of a turret, the flow over it under transonic free stream conditions is quite complex. To study the detailed regime of the transonic flow field over a turret, much experimental and numerical work has been performed (Coirier *et al.* 2014; Vorobiev *et al.* 2014; Beresh *et al.* 2016; De Lucca *et al.* 2018; Kamel *et al.* 2019; Weston and Sherer 2019). Vorobiev *et al.* (2014) studied the relationship between shock and relevant separation in a two-dimensional cylindrical turret in wind tunnel experiments. They found that near the top of the turret, the shock moves upstream and downstream according to the motion of the separation following the shock. Using large eddy simulation (LES), Kamel *et al.* (2019) simulated a wind tunnel experiment conducted by Vorobiev *et al.* (2014) and studied the OPD of the beam emitted at a 105° angle, where the shock wandered around this angle; they found that the OPD mainly fluctuated with the wandering of the shock, apart from the tip component. According to this observation, the OPD could be reduced due to a weakening of the effect of the shock and relevant wake motion through flow control. Gordeyev *et al.* (2010) and Wang *et al.* (2010) identified the effectiveness of passive flow control, which imposes a secondary shear layer from pins to reduce the turbulence intensity of the main shear layer due to the reduction of the OPD under subsonic free stream conditions. Active flow control, unlike passive flow control, involving additional energy brought into the flow field, is also effective for the control of the features of flow (Bhattacharya and Gregory 2015a,b, 2018; Joshi and Bhattacharya 2019; Bhattacharya and Gregory 2020; Bhattacharya and Ahmed 2020) and OPD reduction (Tian *et al.* 2020).

Beresh *et al.* (2016) studied shock motion and related flow fields in the wake of a hemispherical turret using wind tunnel experiments. The shock locations of the 3D turret were different than those of the 2D cylindrical turret. Based on those experiments, Weston and Sherer (2019) studied the shock and wake of a hemispherical turret using delayed detached eddy simulation (DDES). Their results indicated that the wake of the turret in the symmetric plane had the same features, which fluctuated along the wall normal direction, similar to that of the cylindrical turret wake, while another dominant feature at a Strouhal number (St) of about 0.15–0.2 could not be predicted by a 2D cylindrical turret.

Coirier *et al.* (2014) numerically studied the flow field and wavefront distortion of both a hemispherical and a submerged hemispherical turret on a plate with subsonic to supersonic inflow. The results showed a large distortion of the wavefront as the beam transited through the shock region, and the shock located in front of the top of the turret was different from that observed in the 2D cylindrical turret. De Lucca *et al.* (2018) studied the pressure field of transonic flow over a hemisphere tested with pressure-sensitive paint, and the decomposition methods of proper orthogonal decomposition (POD) and dynamic mode decomposition (DMD) were implemented to identify the temporal and spatial characteristics of the flow field. They found that the fluctuation of the wake along the wall-normal direction, which contributed less than the lateral shift of the wake to the flow field, was the second mode feature. Mode decomposition is also used in the study of the features of detailed turret flow, such as in Bhattacharya and Ahmed (2020), which revealed the effects of aspect ratio on the turret flow field using the DMD method.

Kamel *et al.* (2019) showed that shock and separated flow highly affect wavefront distortion. This indicates that studying the effects of dominant wake fluctuation on OPD would provide a basic understanding of the study of flow control to reduce wavefront distortion. Computational fluid dynamics is an effective method of studying the details of a turret flow field. To solve complicated turbulent flow around a 3D turret, the choice of turbulence model is still challenging and needs to be selected carefully. Due to the computational cost of simulating free streams with high Reynolds numbers, LES and even direct numerical simulation (DNS) seem unaffordable (Spalart 2000). The implementation of the Reynolds-averaged Navier–Stokes (RANS) equations can effectively reduce the cost of turbulence simulation; however, the modeled field does not reflect the resolved vortical structures (Szydłowski and Costes 2004; Liu *et al.* 2014), which severely affects the wavefront distortion. Detached eddy simulation, combining the advantages of LES and RANS (Spalart *et al.* 1997, Strelets 2001), and the improved methods of DDES (Menter and Kuntz 2004; Spalart *et al.* 2006) and improved DDES (IDDES) (Shur *et al.* 2008) can resolve the vortical structures of turret flow (Coirier *et al.* 2014; Weston and Sherer 2019; Tian *et al.* 2020). Taking into account that the shielding function of the DDES method may induce a log layer mismatch in the boundary layer, IDDES is competitive for use in simulating the turret flow field.

In this work, the effects of the dominant flow features under transonic conditions on wavefront distortion, knowledge of which is important for the study of flow control, are studied to understand the mechanism of OPD reductions. The transonic flow field over a hemispherical turret is simulated using the IDDES method. To improve the precision of separated flow prediction and vortical structure resolution, a modified sub-grid scale provided by Shur *et al.* (2015) is implemented. The main

components of the wake motions are extracted using the POD method to compare the effects of different flow features on the wavefront distortions. The optical path length (OPL) of the beam is calculated using a third-order Runge–Kutta ray-tracing method, based on the Fermat theorem (Born and Wolf 2013).

2. METHODOLOGY

2.1 Sub-grid Scale of the IDDES Method

This work uses the IDDES method introduced in Shur *et al.* (2008) together with the $k-\omega$ shear stress transfer model (Menter 1994). The sub-grid scale Δ_{SLA} provided by Shur *et al.* (2015) is adopted using the IDDES method. The equation of the sub-grid scale Δ for the IDDES method was suggested by Guseva *et al.* (2017), as follows:

$$\Delta = \min[\max(C_w d_w, C_w \Delta_{\max}, h_{wn}), \Delta_{SLA}], \quad (1)$$

where $\Delta_{\max} = \max(\Delta_x, \Delta_y, \Delta_z)$, indicating the maximum of the distances along the coordinate axes x , y , and z of a grid. d_w is the distance to the wall, the empirical constant C_w is 0.15, and h_{wn} is the wall normal grid spacing. Δ_{SLA} is the modified sub-grid scale, defined as

$$\Delta_{SLA} = \tilde{\Delta}_\omega F_{KH}^{\lim} (<VTM>). \quad (2)$$

As a product of the sub-grid scale $\tilde{\Delta}_\omega$ and a non-dimensional empirical function $F_{KH}^{\lim} (<VTM>)$, Δ_{SLA} sufficiently reduces the sub-grid viscosity at the anisotropic grid, and $\tilde{\Delta}_\omega$ is still insufficient for the required reduction. $\tilde{\Delta}_\omega$ is presented as:

$$\tilde{\Delta}_\omega = \frac{1}{\sqrt{3}} \max_{n,m=1,8} |(I_n - I_m)|, \quad (3)$$

where $I_n = n_\omega \times r_n$, n_ω is the unit vector that is aligned with the vorticity vector, and r_n is the vector of the vertex n to grid cell center. Similarly,

$I_m = m_\omega \times r_m$. $F_{KH}^{\lim} (<VTM>)$ is limited by 1.0 and is presented as:

$$F_{KH}^{\lim} (<VTM>) = \begin{cases} 1.0, & \text{if } (\tilde{f}_d > \varepsilon) \\ F_{KH} (<VTM>), & \text{if } (\tilde{f}_d \leq \varepsilon) \end{cases}, \quad (4)$$

where \tilde{f}_d is the shielding function in the IDDES method, and ε is a constant set to 0.01.

$F_{KH} (<VTM>)$ is as follows:

$$F_{KH} (<VTM>) = \max\{F_{KH}^{\min}, \min\{F_{KH}^{\max}, F_{KH}^{\min} + \frac{F_{KH}^{\max} - F_{KH}^{\min}}{a_2 - a_1} (<VTM> - a_1)\}\}, \quad (5)$$

where $F_{KH}^{\max} = 1.0$ and the values of the adjustable empirical constants F_{KH}^{\min} , a_1 , and a_2 are 0.1, 0.15, and 0.3, respectively. $<VTM>$ denotes the grid averaged vortex tilting measure, defined as:

$$VTM = \frac{\sqrt{6} |(\hat{S} \cdot \omega) \times \omega|}{\omega^2 \sqrt{3 \text{tr}(\hat{S}^2) - [\text{tr}(\hat{S})]^2}} \quad (6)$$

where \hat{S} is the strain tensor, ω is the vorticity vector, and $\text{tr}(\cdot)$ is the trace.

2.2 POD Algorithm

According to the Gladstone–Dale relation (Wolfe and Zizzis 1978), the refractive index is mainly affected by flow density. The snapshot POD, clearly introduced in the work of Taira *et al.* (2017), is used to decompose a series of density field snapshots with a fixed time interval. Assuming that there are N snapshots, and each contains M spatial nodes, where $N \ll M$ for 3D flow field, snapshot \mathbf{u}_i can be written as:

$$\mathbf{u}_i = \frac{1}{N} \sum_{j=1}^N \mathbf{u}_j + \mathbf{v}_i, \quad (7)$$

where \mathbf{v}_i denotes the fluctuating form of the flow field and is presented as:

$$\mathbf{v}_i = \sum_{j=1}^N a_j(i) \mathbf{p}_j, \quad (8)$$

where $\mathbf{p} = (\mathbf{p}_1, \dots, \mathbf{p}_N)$ is the POD modes, and $a_j(i)$ is the mode coefficient, which expresses the mode evolution over time of mode j at the time snapshot of i .

In the algorithm, matrix \mathbf{C} is defined as $\mathbf{C} = \mathbf{V}^T \mathbf{V}$, and the dimension of $\mathbf{V} = \{\mathbf{v}_1, \dots, \mathbf{v}_N\}$ is $N \times N$. The eigenvalue of \mathbf{C} is acquired by:

$$\mathbf{C} \mathbf{A}_j = \lambda_j \mathbf{A}_j, \quad (9)$$

where $\mathbf{A}_j = [a_j(1), a_j(2), \dots, a_j(N)]^T$ is the matrix of the mode coefficient. The POD mode \mathbf{p}_j can be calculated as:

$$\mathbf{p}_j = \frac{1}{\sqrt{\lambda_j}} \mathbf{V} \mathbf{A}_j. \quad (10)$$

The normalized energy is presented as:

$$E_i = \lambda_i / \sum_{j=1}^N \lambda_j. \quad (11)$$

2.3 Ray-tracing Method

Relevant turret angles and a beam transmission are shown in Fig. 1. Az and El , representing the azimuthal and elevation angles, are most commonly used to describe the location of the optical window.

For convenience, viewing angle α and modified elevation-plane angle β are used to describe the beam

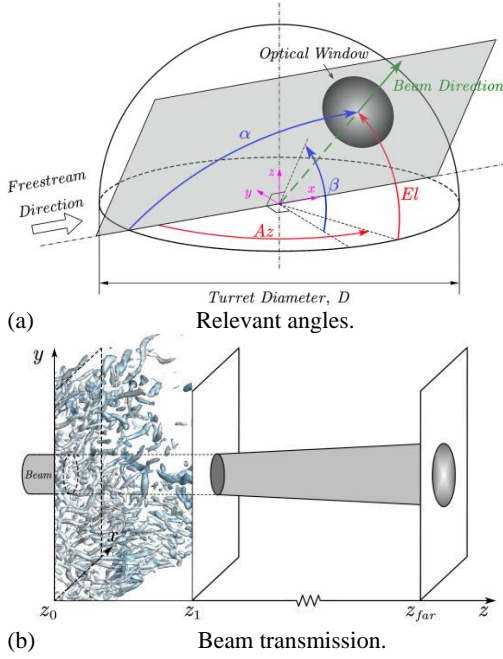


Fig. 1. Schematics of the angles and beam transmission of the turret.

direction from the flow point of view (Gordeyev and Jumper 2010; Porter *et al.* 2013). The relations of these angles are presented as:

$$\begin{aligned} \alpha &= \cos^{-1}(\cos(Az) \cos(El)) \\ \beta &= \tan^{-1}(\tan(El) \sin(Az)) \end{aligned} \quad (12)$$

The beam emitted from the optical window, located at z_0 in Fig. 1(b), is transmitted through the turbulent region, where the distance is from z_0 to z_1 , with the same order of magnitude as the turret diameter. As the wavefront is distorted at z_1 , the intensity distribution of the beam transmitted from z_1 to z_{far} , which denotes an undisturbed atmospheric environment in which the distance is much farther than that from z_0 to z_1 , will be severely affected (Tian *et al.*, 2020). A third-order Runge–Kutta ray-tracing method is used in this work to calculate the OPL of each ray.

OPD, which represents the wavefront distortion, is calculated as follows:

$$OPD = OPL - \langle OPL \rangle, \quad (13)$$

where the angle brackets denote the average value. OPL is calculated by

$$OPL = \int_0^L n ds, \quad (14)$$

where n is the local refractive index and can be calculated by $n = 1 + K_{GD} \rho^*$ (Gladstone and Dale 1863), where ρ^* is the density and K_{GD} is the Gladstone–Dale coefficient.

As the flow field can be treated as stationary in relation to beam transmission, the beam transmitted through each time snapshot can be traced as:

$$\frac{d}{ds} \left(n \frac{dr}{ds} \right) = \nabla n. \quad (15)$$

For the third-order Runge–Kutta method, Eq. (14) can be written as:

$$\begin{cases} \frac{dT}{ds} = \nabla n \\ \frac{dr}{ds} = \frac{1}{n} T \end{cases}, \quad (16)$$

where the relevant parameters are defined as:

$$r = \begin{pmatrix} x \\ y \\ z \end{pmatrix}, T = \begin{pmatrix} T_x \\ T_y \\ T_z \end{pmatrix} = n \begin{pmatrix} \frac{dx}{ds} \\ \frac{dy}{ds} \\ \frac{dz}{ds} \end{pmatrix}, D = n \begin{pmatrix} \frac{\partial n}{\partial x} \\ \frac{\partial n}{\partial y} \\ \frac{\partial n}{\partial z} \end{pmatrix}, \quad (17)$$

where x , y , and z represent the coordinates, and s is the ray path.

Finally, the third-order Runge–Kutta form of the ray-tracing method is as follows:

$$\begin{cases} r_{m+1} = r_m + \Delta t \left[T_m + \frac{1}{6}(A + 2B) \right] \\ T_{m+1} = T_m + \frac{1}{6}(A + 4B + C) \end{cases}, \quad (18)$$

where the values of A , B , and C can be calculated by:

$$\begin{cases} A = \Delta t D(R_m) \\ B = \Delta t D \left(R_m + \frac{\Delta t}{2} T_m + \frac{\Delta t}{8} A \right) \\ C = \Delta t D \left(R_m + \Delta t T_m + \frac{\Delta t}{2} B \right) \end{cases}, \quad \Delta t = \frac{\Delta s}{n} \quad (19)$$

The tracing length step Δs is determined as an empirical relation of the variation in refractive index that is also implemented in the work of Tian *et al.* (2020), and is as follows:

$$\Delta s = f(x_g) = \begin{cases} \Delta_i, & x_g < 10^{-7} \\ 0.5\Delta_i, & 10^{-7} < x_g \leq 10^{-6} \\ 0.2\Delta_i, & 10^{-6} < x_g \leq 10^{-5} \\ 0.1\Delta_i, & 10^{-5} < x_g \leq 10^{-4} \\ 0.05\Delta_i, & x_g > 10^{-4} \end{cases}, \quad (20)$$

where x_g is the variation in refractive index among the adjacent nodes, and Δ_i is the average-length scale of the local grid and is calculated using the equation of

$\Delta_i = \sqrt[3]{l_i \times l_j \times l_k}$, where l_i , l_j , and l_k are the length scale of the grid along three directions.

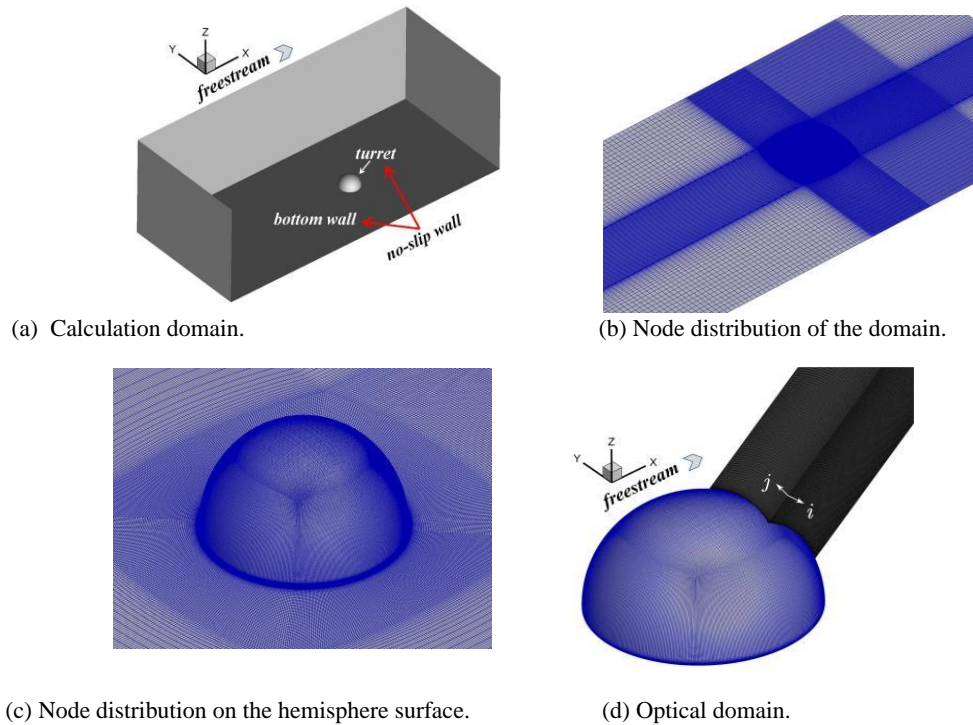


Fig. 2. Description of simulation domain and the distribution of the grid.

2.4 Numerical Set-up

The simulation is conducted through a multi-block structured grid and using the RANS-based code CFL3D. To predict the transonic flow field around a 3D hemispherical turret, the inviscid term is discretized with the Roe scheme, which is a flux difference splitting method. The flux of the Roe scheme is reconstructed using a fifth-order WENO scheme. A central scheme is implemented to discretize the viscous term. The LU-SGS implicit algorithm with a pseudo time iteration is implemented for time matching.

The calculation condition is set to match the experiment conducted by Beresh *et al.* (2016) and the simulation conducted by Weston and Sherer (2019). The diameter of the hemisphere (D) is 76 mm. A multi-block grid with an O-type topology is used in the current flow field simulation, and the descriptions of the simulation domain and relevant grid distribution are presented in Fig. 2. Three grids with certain detailed parameters shown in Table 1 are applied to the study of the grid resolution. The heights of the first layer nodes are set to $5 \times 10^{-6} D$ to make a Y^+ of about the order of 1. The hemispherical turret and the bottom wall are set as no-slip walls, and the rest are treated as free stream boundaries. The free stream Mach number M_∞ and the Reynolds

number based on the turret diameter are set as 0.8 and 1.3 million, respectively. The dimensional time step is about $5 \times 10^{-7} s$.

3. RESULTS AND DISCUSSION

3.1 Grid Resolution and Field Validation

To clarify the grid resolution, Fig. 3 shows comparisons of different grid cases. The average and maximum Y^+ values are about 0.3 and 0.8 for all cases. The comparison of the dimensionless density $\rho = \rho^* / \rho_\infty^*$, which is monitored for 24000 iterations (after running a massive number of preliminary iterations) to acquire steady periodical flow features, is presented in Fig. 3(a); here, ρ^* is the local dimensional density and ρ_∞^* is the dimensional free stream density. The direction of the monitoring location is described by α and β , which are 85° and 0.57° , respectively. The distance between the monitoring location and the center of the hemisphere is $0.525 D$. The monitored density curves of the medium and fine grid cases match each other well. The coarse grid fails to predict the amplitude and period. Fig. 3(b) presents the mean velocity profiles of the incoming boundary layer, acquired $0.833 D$ upstream of the turret. The experimental result provided by Beresh *et al.* (2016) is also compared. U/U_∞ indicates the ratio of the streamwise velocity and the free stream velocity. z/δ indicates the ratio of the z coordinate and the boundary layer thickness δ . The velocity profiles at $0.833 D$ upstream of the turret are nearly time-independent and are unchanged, and the boundary layer thickness is about $0.176 D$. The velocity

Table 1 Grid information for different grids

Grid	Total nodes	Circumferential nodes of the hemisphere
Coarse	8 million	352
Medium	23 million	520
Fine	66 million	744

profiles and the boundary layer thickness match experimental data well, except for the coarse grid, which severely overestimates the velocity in the boundary layer. Fig. 3(c) shows the mean pressure coefficient (C_p) curves measured at the turret surface. These numerical data are collected in the plane in which β is 90° . As pressure coefficients were not measured by Beresh *et al.* (2016), the in-flight experimental data collected at an altitude of 28,000 feet with $Ma=0.8$ and a Reynolds number of about 2.4 million based on the turret diameter reported by Morrida *et al.* (2016) are compared for reference. Although all of the grids seem to predict the C_p well, the result of the coarse grid case is obviously different. The medium grid can precisely predict the basic features of the flow field, so the following discussion is based on the medium grid.

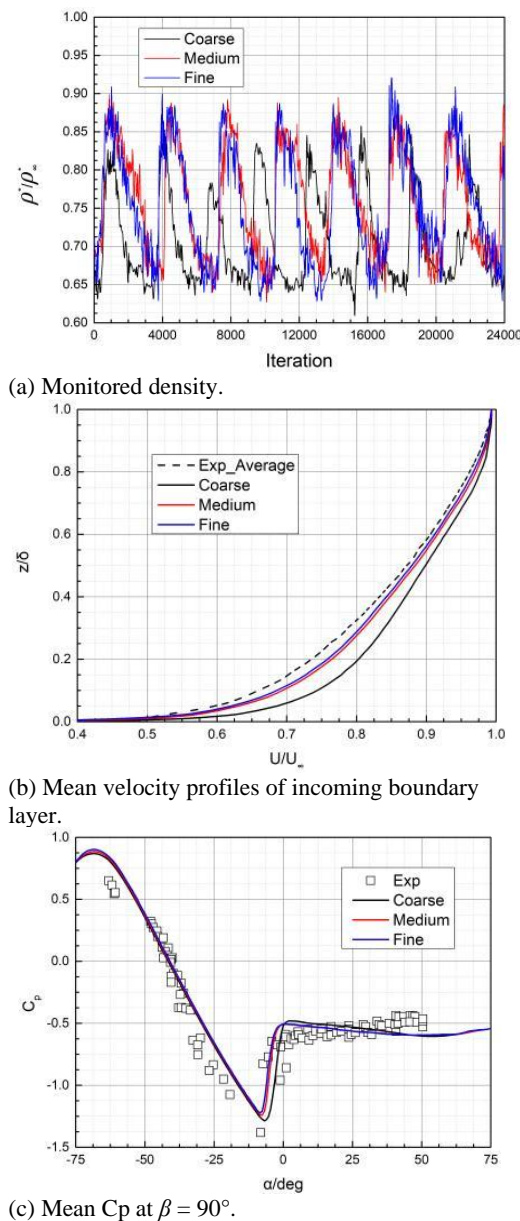


Fig. 3. Comparisons of results from different grid cases.

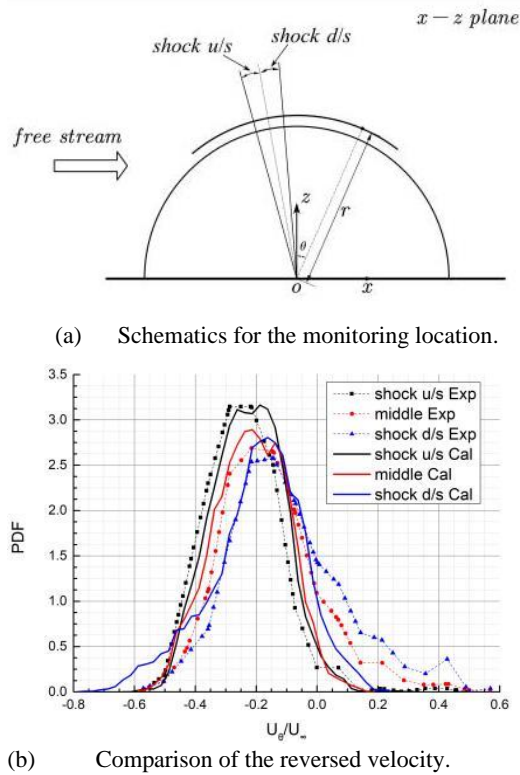
Figure 4 presents a comparison of the reversed flow velocity between numerical results, collected from the 24000 iterations shown in Fig. 3(a), and experimental data provided by Beresh *et al.* (2016). The schematics of the monitoring location are shown in Fig. 4(a), and 4(b) indicates the probability density function (PDF) of the tangential velocity in the x - z plane near the surface of the hemisphere with a distance $r=0.525 D$. The range of the monitoring angle θ is from 30° to 40° . U_θ in Fig. 4(b) denotes the local velocity. The shock foot (the shock at a height of $0.525 D$) located upstream is denoted as shock u/s, while the one located downstream is denoted as shock d/s. The shock foot located between $-0.5 \sigma_r$ and $0.5 \sigma_r$ is denoted as the middle, where σ_r is the standard deviation of shock foot positions. The PDF of the tangential velocity indicates well-matched statistical data, while some discrepancies are observed in the curve of the middle and shock d/s, where the simulated reversed flow is slightly more than that of experimental data. These discrepancies were also observed by Weston and Sherer (2019), who considered that the mismatch between the numerical and experimental set-up was not negligible. Therefore, we conclude that the simulation can properly predict the transonic flow features over the turret.

3.2 Flow Features and Wavefront Distortions

To schematically understand the flow behind the shock and the dominant wake motion features, Fig. 5 presents the flow field from two different views. Fig. 5(a) and 5(b) present a vertical view, while 5(c) and 5(d) present a side view. The turbulent structures are expressed through the Q criterion introduced by Jeong and Hussain (1995):

$$Q = -\frac{1}{2} \left[\left(\frac{\partial u}{\partial x} \right)^2 + \left(\frac{\partial v}{\partial y} \right)^2 + \left(\frac{\partial w}{\partial z} \right)^2 \right] - \left(\frac{\partial u}{\partial y} \right) \left(\frac{\partial v}{\partial x} \right) - \left(\frac{\partial u}{\partial z} \right) \left(\frac{\partial w}{\partial x} \right) - \left(\frac{\partial v}{\partial z} \right) \left(\frac{\partial w}{\partial y} \right), \quad (21)$$

where u , v , and w are velocity along the coordinate axes x , y , and z , respectively. The contours of all figures are colored according to the dimensionless density ρ . The flow shown in Fig. 5(a) and 5(b) denotes a wake lateral shift feature along with the shock located upstream and downstream alternatively. For example, on the side with the black arrow, the shock shown in Fig. 5(a) is located upstream, while the shock at another side is located downstream. The background planes in Fig. 5(a) or Fig. 5(b) are also colored by dimensionless density and are parallel to the bottom wall, with a distance of $0.5 D$. Massive turbulent structures moving with fluctuations in the wake are also observed, while the flow field at the upstream side of the turret is quite steady. The features of the wake fluctuation shown in Fig. 5(c) or Fig. 5(d) are similar to those of the 2D cylindrical turret (Kamel *et al.* 2019). Obviously, the wake fluctuates in the wall-normal direction along with the shock at the top of the turret moving upstream and downstream. The flow field at the



(a) Schematics for the monitoring location.
 (b) Comparison of the reversed velocity.
Fig. 4. Reversed tangential velocity of different shock foot locations.

upstream side of the turret indicates a steady refractive index distribution, with the exception of the region near the bottom, where the so-called necklace vortex exists. As a large field of regard of the turret is affected by the shock and the wake, several beams transmitted through the shock and wake regions are studied here. Angles α and β of these beams are presented in Table 2.

The distances for all beam transmissions are set to 1 D , and the diameter of each beam is 0.325 D . The grid

scale in the optical domain is strictly controlled to match the medium grid. For convenience, the optical domain is built by extending a square where the nodes and the grid length are kept the same on both sides. The extended direction is the same as the direction of beam propagation, and the coordinates i and j denote the two sides of a square, as shown in Fig. 2(d). The grid growth ratio is controlled according to the flow field grid growth, and the optical domain contains about 3.3 million nodes.

In Fig. 3(a), 450 snapshots from about iterations 16000 to 24000 are shown, with a fixed time interval of about 9×10^{-6} s; these are used to study the wavefront distortions. Considering the Mach number dependence (Porter *et al.* 2013), it is convenient to use a normalized OPD, denoted as OPD_{Norm} , instead of the OPD. The OPD_{Norm} is normalized as:

$$OPD_{Norm} = \frac{OPD}{\left(\rho_{\infty}^* / \rho_{SL} M_{\infty}^2 D\right)}, \quad (22)$$

where ρ_{SL} is the density at sea-level.

To understand the wavefront distortions of the beams presented in Table 2, Fig. 6 shows the temporal features of the root mean square (RMS) of the spatial OPD_{Norm} , denoted as $OPD_{rms,s}$. The curves presented at the top of Fig. 6(a) express the evolution of $OPD_{rms,s}$, while the OPD_{rms} shown in Fig. 6(b) denotes the RMS of the temporal curve of $OPD_{rms,s}$. OPD_{ave} indicates the time-averaged value of the $OPD_{rms,s}$. Fourier series expansion is implemented to study the frequency characteristics of $OPD_{rms,s}$ curves. The relation of amplitude and Strouhal number is shown at the bottom of Fig. 6(a). According to Fig. 6(a), for all of the beams, the curves of $OPD_{rms,s}$ fluctuate periodically, although the amplitudes are quite different because of the differences in beam path. According to the $OPD_{rms,s}$

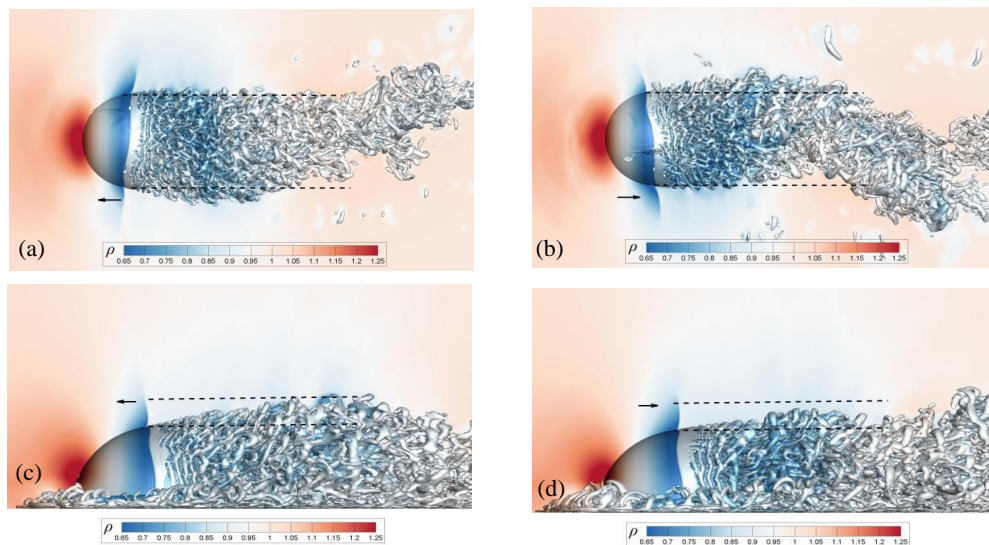


Fig. 5. Schematics of the wake motion: (a) Wake lateral shift of shock u/s on the black arrow side, (b) Wake lateral shift of shock d/s on the black arrow side, (c) Wake wall normal fluctuation of shock u/s, (d) Wake wall normal fluctuation of shock d/s.

Table 2 Relevant angles of different beams

Beam	$\alpha, ^\circ$	$\beta, ^\circ$
Beam 1	100	90
Beam 2	110	90
Beam 3	120	90
Beam 4	130	90
Beam 5	140	90
Beam 6	111	51

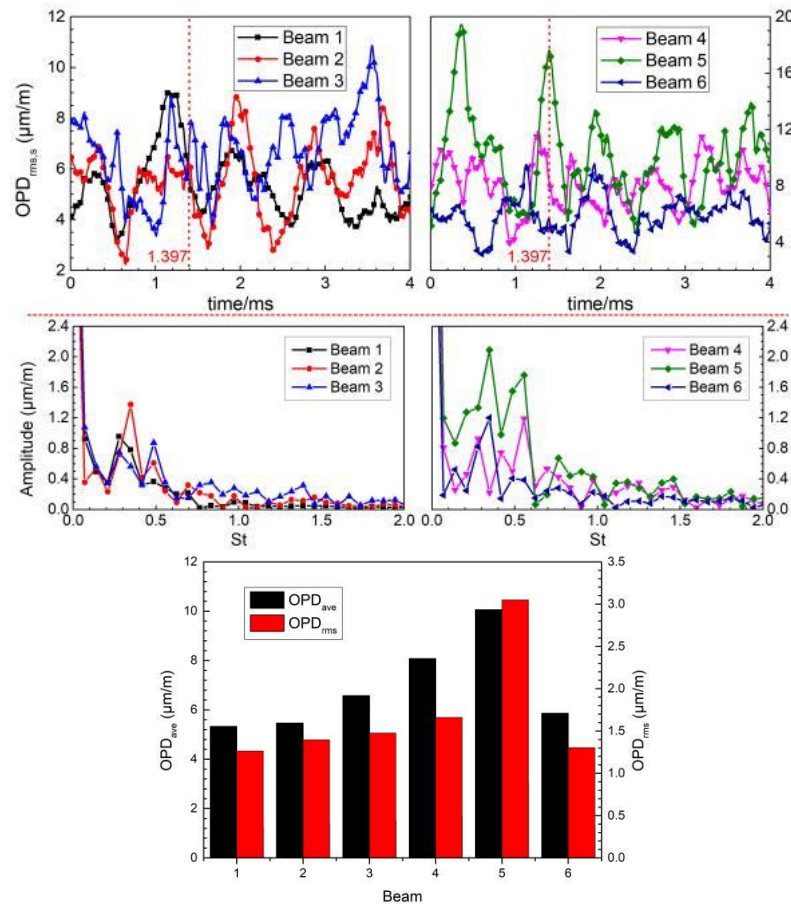
of beams 1 to 5, the $OPD_{rms,s}$ fluctuates more severely as α increases, which indicates that the large-scale turbulent structures in the wake severely affect the wavefront. The wavefront of beam 6 is quite similar to that of beam 2, as their viewing angles are almost the same and the modified elevation angle β for beam 6 continues to be large enough so that the beam is affected by flow features that also affect beam 2. Generally, the mean flow of variables around a sphere is a function of the viewing angle only (Porter *et al.* 2013). The amplitude determined using Fourier series expansion shows that for all beams the range of high amplitude is mainly below $St=0.6$, which indicates that the $OPD_{rms,s}$ is most affected by the density variation induced by large scales, and the low-frequency structures and the control of the relevant flow features may be effective for the reduction of

wavefront distortion. The time-averaged $OPD_{rms,s}$, denoted as OPD_{ave} and presented in Fig. 6(b), shows the same regularity as OPD_{rms} does. OPD_{ave} and OPD_{rms} increase rapidly with α . It should be mentioned that the values of OPD_{Norm} are larger than the experimental data provided by Morrida *et al.* (2016) because all parts of the wavefront distortions are included in the current work.

To schematically assess the spatial distribution of OPD_{Norm} , Fig. 7 shows the OPD_{Norm} distributions of beams 1 and 5 at 1.397 ms, where the amplitude curve of beam 5 presented in Fig. 6(a) shows a peak. The OPD_{Norm} of beam 1, shown here, is used to schematically study the effects of shock on wavefront distortion. As beam 1 is transmitted through the shock region, OPD_{Norm} grows rapidly after the shock, as the density behind the shock grows dramatically. OPD_{Norm} of beam 5, presented in Fig. 7(b), shows very similar features to the turbulent structures. The OPD_{Norm} distributions in both figures are obviously asymmetric. This is caused by an asymmetric density field, which may be affected by the lateral motion of the wake.

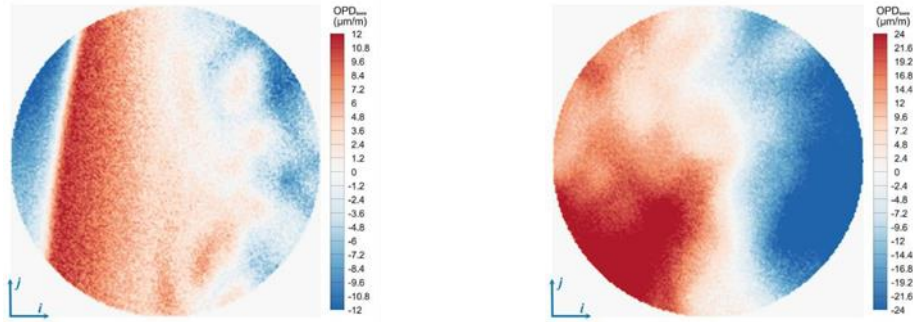
3.3 POD Mode Analysis

To enable study of the POD modes, Fig. 8 presents the cumulative energy limited to the first 200 modes. The first 4 and the first 20 modes contain about 12%



(a) Temporal evolution of $OPD_{rms,s}$. (b) Averaged and RMS value of $OPD_{rms,s}$.

Fig. 6. Wavefront distortions of different beams.



(a) OPD_{Norm} of beam 1.

(b) OPD_{Norm} of beam 5.

Fig. 7. OPD distributions of beams 1 and 5 at 1.397 ms.

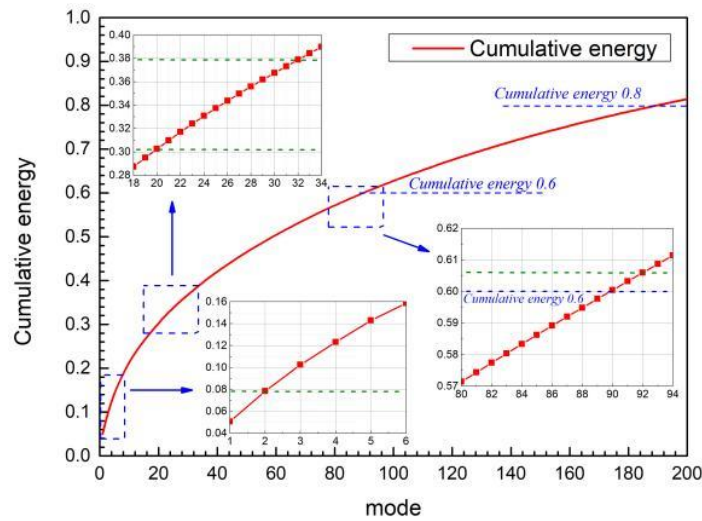


Fig. 8. POD cumulative energy limited to the first 200 modes.

and 30% of the density field energy, respectively. In addition, the first 100 and the first 200 modes contribute more than 60% and 80% of the energy to the flow field, respectively.

To enable study of the dominant spatial features of the density field, the first six modes are presented in Fig. 9. The figure at the top left corner for each mode is the contour on the x - z plane and the bottom plane is parallel to the bottom wall with a distance of $0.025 D$. Four spatial planes parallel to the y - z plane with distances of $0.5 D$, $1.43 D$, $2.36 D$, and $3.29 D$ to the turret center are used to present the spatial features in the wake. The mode energy is shown in the bottom right corner. Modes 1 and 2 mainly show a dominant feature of the wake lateral shift (spatially asymmetric). Another dominant feature of the wake fluctuating along the wall-normal direction (spatially symmetric) is quite clear in mode 4. Although mode 3 also features wake wall-normal fluctuation, it seems to contain other components of wake motion. The spatial feature located upstream of the turret, which indicates the necklace vortex, exists in the first four modes, and it is very clear in modes 3 and 4. The features of the first four modes are dominant in the flow field and are quite similar to those provided by De Lucca *et al.* (2018). Modes 5 and 6 seem to contain the components of the lateral shift and the

wall-normal fluctuations of the wake. These results suggest that in addition to the first four modes, several lower-order modes need to be considered in the analysis of the effect of these two dominant features, namely, the lateral shift and the wall-normal fluctuation of the wake, on the wavefront distortions. Another reason for this is that the wake lateral shift contributes no more than 7.844% mode energy to the total field if only modes 1 and 2 are considered. The wall-normal fluctuation of the wake contributes no more than 4.488% of the mode energy to the total field if only modes 3 and 4 are considered. The wavefront distortion may not be obvious, for example, if modes 3 and 4 are removed from the density field. It should be noted that the necklace vortex can still be observed in modes 5 and 6. In addition, the shock can be observed in all of the first six modes.

Figure 10 presents several higher-order modes to study the relevant spatial features. As the order of the modes grows, the contribution of the mode to the total flow becomes weaker. It can be seen that modes 10 and 15 contain the components of both dominant features of the wake lateral shift and wall-normal fluctuation. The shock and the necklace vortex can also be observed in both modes, but the smaller-scale structures are more obvious. Modes 20

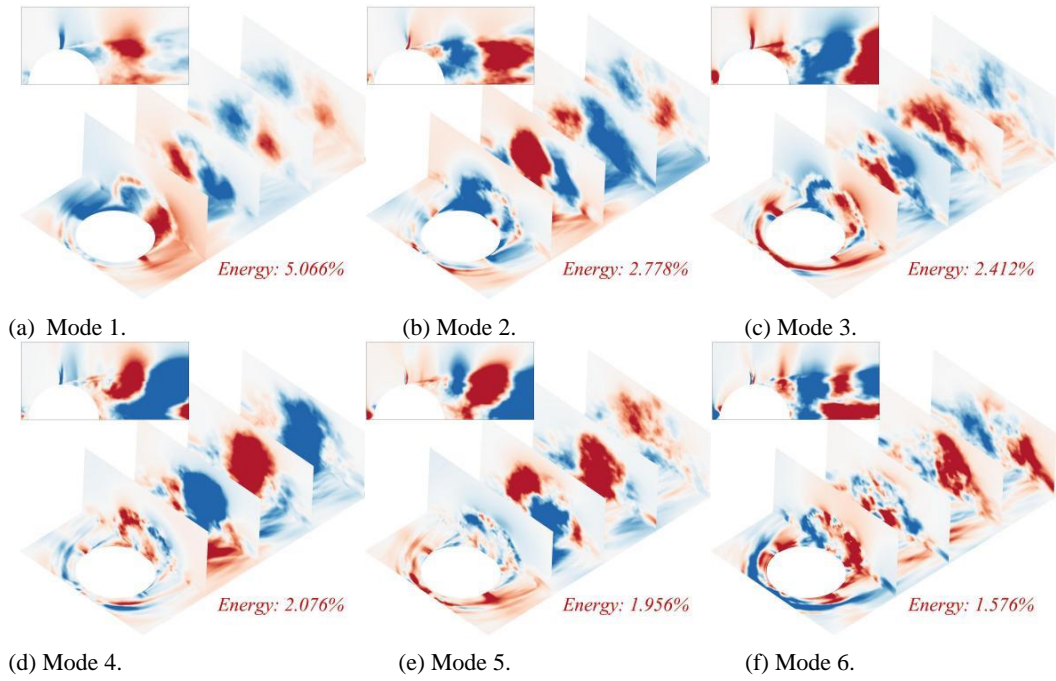


Fig. 9. Spatial distribution of the lower-order modes from mode 1 to mode 6.

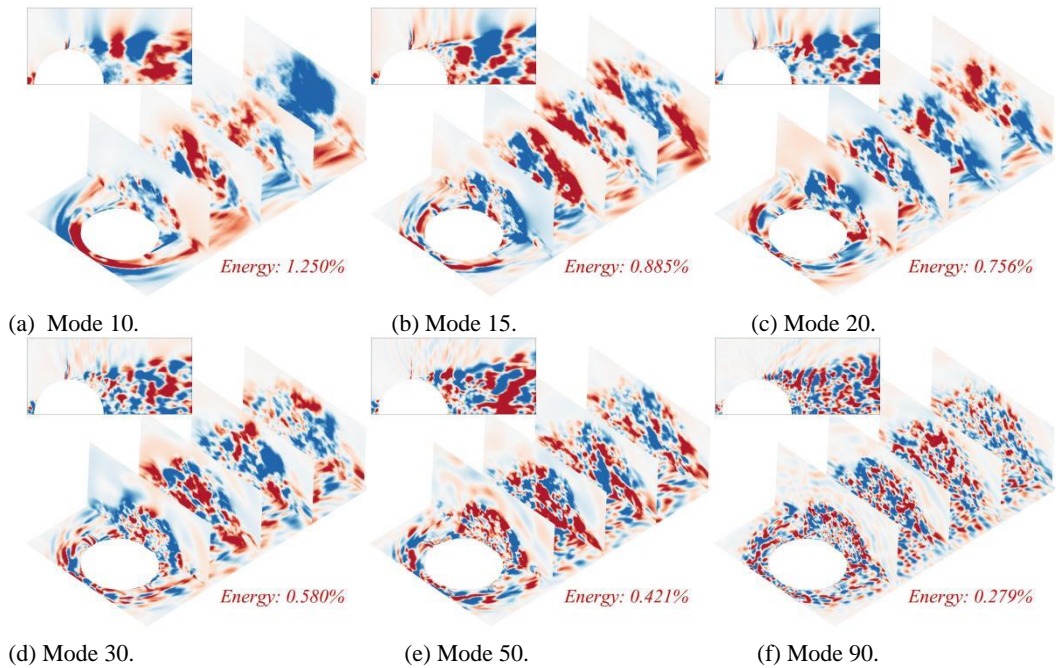


Fig. 10. Spatial distribution of the higher-order modes.

and 30 present disordered distributions of spatial features. The shock in both modes becomes weaker, and massive smaller-scale structures are observed in the necklace vortex region compared to those in modes 10 and 15. The spatial structures presented in mode 50 become smaller, and the shock almost disappears. Mode 90 presents extremely small-scale structures and only contains 0.279% of the total mode energy. According to the spatial distribution from modes 1 to 90, a comparison of the wavefronts of beams transmitted through the flow fields, which remove the modes containing larger-scale and smaller-scale structures from the initial field,

respectively, is effective for studying the wavefront distortions caused by different dominant features and can help clarify flow control to reduce wavefront distortion.

Figure 11 presents the coefficients and their Fourier series expansions of the modes shown in Figs. 9 and 10 to study the evolutions of the POD modes. The temporal characteristics presented in Fig. 11(a) indicate that modes 1 and 2 mainly fluctuate at an St range of 0.07–0.2, and the St of the maximum amplitude is about 0.15. This indicates that the wake shifts laterally at about $St=0.15$. The mode coefficients of modes 3 and 4 show different

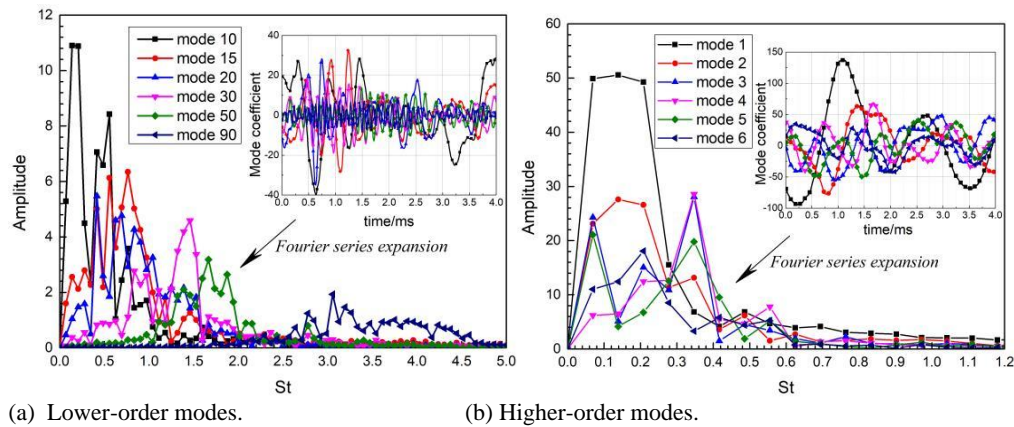


Fig. 11. Temporal characteristics of relevant modes.

temporal features, where the amplitudes of both modes are quite low, at $St=0.15$, and the maximum amplitudes of both modes are found at about $St=0.35$. This indicates that the feature of the wall-normal fluctuation mainly fluctuates at about $St=0.35$, and according to the variation in $OPD_{rms,s}$, shown in Fig. 6, the large amplitude at $St=0.35$ for each beam should be related to the wall-normal fluctuation of the wake. The amplitude of mode 3 still shows a high value at about $St=0.07$. This high amplitude matches the wake lateral shift component in mode 3. Unlike the first four modes, the overall amplitudes of modes 5 and 6 decrease as their contributions to the flow field decrease, while they still contain the components of two dominant features of the wake, according to their amplitudes at low St values. The mode coefficients of higher-order modes shown in Fig. 11(b) indicate that the high-amplitude region moves to the high- St region as the mode order increases. Mode 10 obviously contains low- St features, while the high amplitudes of mode 15 and mode 20 are found mainly at the range of $St=0.5-1.0$. The low- St features in mode 30 seem to fall sharply and they almost disappear by mode 50. Mode 90 indicates that higher amplitudes are mainly in the range of $St=2.5-4.5$. The mode coefficients also validate the existence of the necklace vortex in the related POD modes, as the DMD performed by De Lucca *et al.* (2018) showed that the necklace vortex exists at $St=0.2$ and $St=1.0$.

3.4 Effects of Flow Features on Wavefront Distortions

According to the spatial features presented in Figs. 9 and 10 and the temporal characteristics presented in Fig. 11, three flow fields are reconstructed to study the effects of the dominant features of flow on wavefront distortions. As mode 20 contains low- St components, a flow field with the first 20 modes removed is provided to present the effects of smaller-scale structures on the wavefront distortion. Considering that the first 20 modes contribute about 30% of the energy to the total flow field, modes 3 to 32, which also contain 30% of the energy, are removed to study the effect of the wake lateral shift on the wavefront distortion. Modes 21 to 92, containing the same energy, are removed as a

comparison to study the effect of larger-scale structures. These three flow fields are presented in Table 3 and are called fields 2, 3, and 4, respectively. For comparison, field 1 is the initial field without any mode removed.

Table 3. Descriptions of different reconstructed density fields.

Density field	POD modes removal
Field 1	No mode removed (Original field)
Field 2	Modes 1–20 (30% energy) removed
Field 3	Modes 3–32 (30% energy) removed
Field 4	Modes 21–92 (30% energy) removed

Figure 12 presents the amplitude of the Fourier series expansion of $OPD_{rms,s}$ for each beam transmitted through different fields. The time-averaged value and RMS of $OPD_{rms,s}$ are also shown in Fig. 12. According to Fig. 12(a), when beam 1 is transmitted through field 4, the amplitude curve is almost unchanged when St is lower than 0.25. A slight decrease in amplitude can be observed at about $St=0.3$, while a significant change in amplitude is observed in the range of $St=0.45-0.9$, where the amplitude decreases about $0.17 \mu\text{m/m}$ at $St=0.48$ and increases about $0.17 \mu\text{m/m}$ at $St=0.76$. This indicates that removing modes 21 to 92 leaves the low-frequency components of $OPD_{rms,s}$ unchanged, as the features of the lower-order modes (modes 1 to 20) are still in the path of beam 1. Compared to the beam transmitted through field 4, beam 1 transmitted through field 2 produces a very different amplitude distribution of $OPD_{rms,s}$. An obvious change is that, with a decrease of $0.85 \mu\text{m/m}$, the peak amplitude around $St=0.28$ almost disappears, and the amplitude remains at a low level in the low- St region, where St is lower than 0.45. An increase in amplitude is observed where St is above 0.45, which indicates that the effects of lower-order modes are weaker when St is above 0.45. While field 2 removes the opposite modes in the same way that field 4 does, the characteristics of $OPD_{rms,s}$ show an important effect of the dominant flow features, including the wake lateral shift and wall-normal fluctuation, as well as large-scale structures of the flow field on the wavefront distortion. Field 3, with modes 3 to 32 removed, is provided to present the effect of the wake

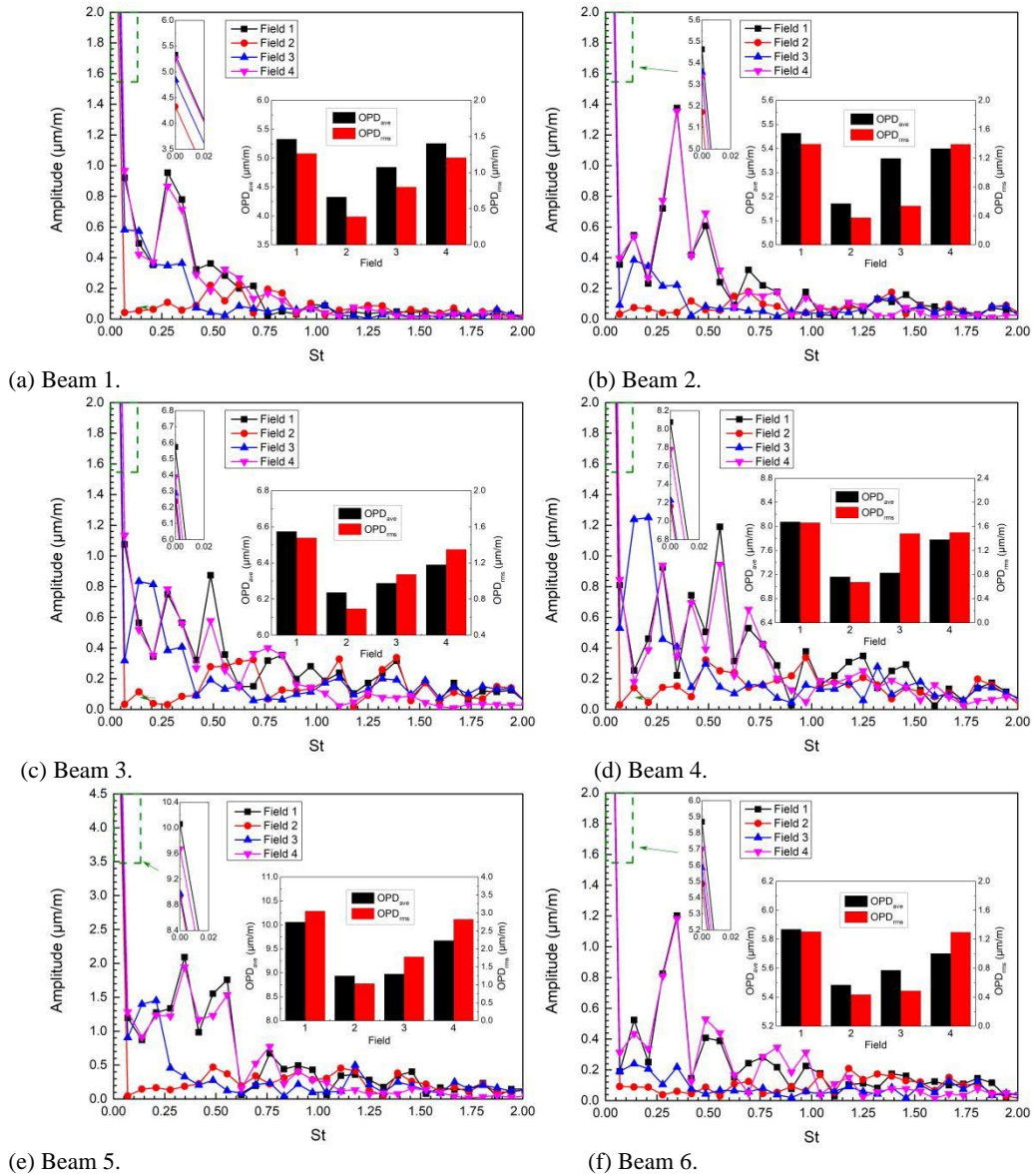


Fig. 12. Fourier series expansion of $OPD_{rms,s}$ of beams transmitted through different fields.

lateral shift on the wavefront distortion. The amplitude of beam 1 transmitted through field 3 shows a relatively different characteristic of $OPD_{rms,s}$. As the components of modes 1 and 2 exist in field 3, amplitudes at St below 0.2 are similar to those in fields 1 and 4, although a slight difference is observed at $St=0.07$ because the removed modes of field 3 still contain the components of low St . As the wavefront of beam 1 transmitted through field 4 is slightly changed, which confirms that the effect of modes 21 to 32 on wavefront distortion is limited, the wake lateral shift seems to seriously affect the fluctuation of $OPD_{rms,s}$ at low St , according to the amplitude curves of fields 2 and 3. In addition, the amplitude at an St of about 0.35 obviously decreases after removing the component of the wake wall-normal fluctuation. An interesting observation can be seen at $St=0.45-0.9$, where the amplitude of field 3 is small, and seems to be comprehensively affected by modes 3 to 32. The values of OPD_{ave} of beam 1 transmitted through fields 2, 3, and 4 fall about 18.8%, 9.1%, and 1.4%, respectively, while the

values for OPD_{rms} fall about 69.1%, 36.8%, and 4.6%, respectively. According to this analysis, the large-scale structures, including the dominant features (namely, lateral shift and wall-normal fluctuation of the wake), are the main reason for the wavefront distortion of the beam transmitted through the shock-affected region. The flow control that forces large-scale structures to be smaller contributes to reducing the wavefront distortion of the relevant region.

Figure 12(b) shows the parameters related to the wavefront distortion of beam 2. Compared to the amplitude curves of beam 1, those of beam 2 indicate that the wall-normal fluctuation of the wake has a significant influence on the $OPD_{rms,s}$ due to the high amplitude at $St=0.35$. As with beam 1, beam 2, when transmitted through field 4, produces a wavefront distortion similar to that of which occurs during transmission through field 1. This indicates the reduced influence of the smaller-scale structures presented in higher-order modes on wavefront

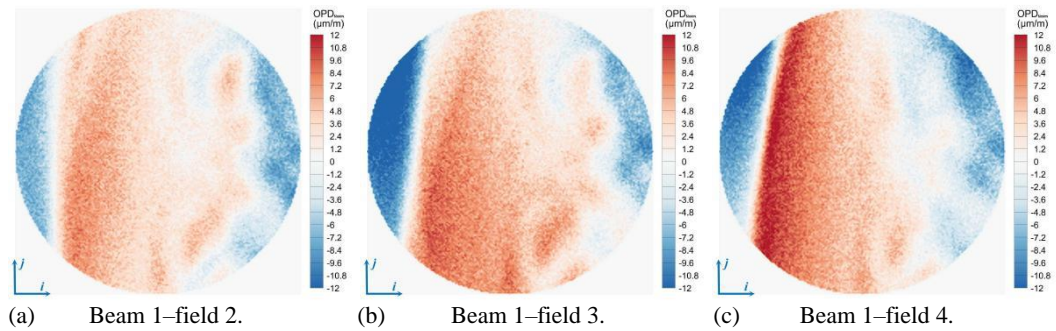


Fig. 13. OPD_{Norm} distribution of beam 1 transmitted through different fields.

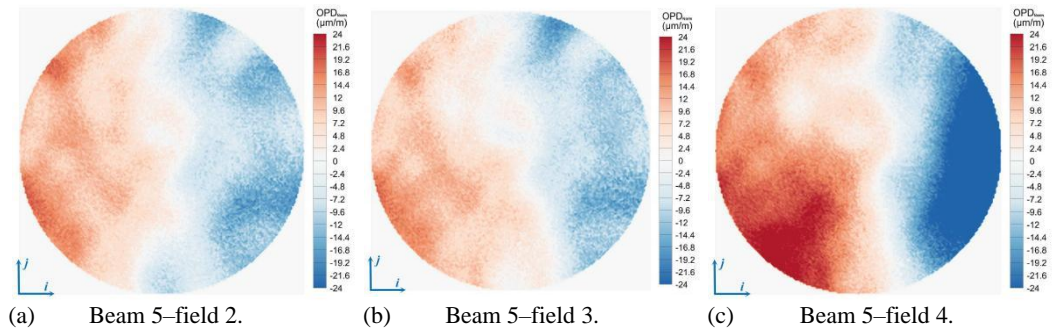


Fig. 14. OPD_{Norm} distribution of beam 5 transmitted through different fields.

distortion. When beam 2 is transmitted through field 3, the amplitude below $St=0.2$ is recovered due to the existence of the lateral shift component of wake. Although the path of beam 2 is far from the shock region, relative to beam 1, the dominant flow features and large-scale structures have similar effects on wavefront distortions. Relative to beam 2, transmitted through field 1, the OPD_{ave} values of beam 2, transmitted through fields 2, 3, and 4 fall about 5.3%, 1.9%, and 1.4%, respectively, while the values of OPD_{rms} fall about 73.2%, 61.5%, and 2.9%, respectively.

Figure 12(c), 12(d), and 12(e) present the wavefront distortions of beams 3, 4, and 5, respectively. The paths of the three beams move gradually away from the shock region. For these three beams, a similar feature is found; that is, without the adjustment of the components in modes 3 to 32, the lateral shift of the wake seriously affects the wavefront distortion, as the amplitude of $OPD_{rms,s}$ is extremely large at about $St=0.15$. This is based on the amplitude curves of field 3, particularly for beam 4, where the amplitudes of field 3 at $St=0.14$ and $St=0.21$ are about $0.98 \mu\text{m/m}$ and $0.78 \mu\text{m/m}$ larger than those of field 1, respectively. Although the flow features presented in the lower-order modes have a major influence on the wavefront distortion according to the OPD_{ave} of each beam transmitted through field 2 (where the OPD_{ave} values of beams 3, 4, and 5 are reduced about 5.1%, 11.3%, and 11.2%, respectively), the effect of modes 1 and 2 on the averaged $OPD_{rms,s}$ seems to be limited (as the OPD_{ave} values of beams 3, 4, and 5 are 4.4%, 10.5%, and 10.8% when transmitted through field 3). However, according to the values of OPD_{rms} , the wake lateral shift severely affects the fluctuation of the variation in $OPD_{rms,s}$. It should be noted that the

irregularities observed in Fig. 12(c), 12(d), and 12(e) are highly correlated with the flow field structures. For example, beams 4 and 5 pass through the initial field and produce different amplitudes at $St=0.35$ and 0.48.

Figure 12(f) shows the wavefront distortion of beam 6. The amplitude at $St=0.35$ is reduced considerably when the lower-order modes are removed. When this beam passes through fields 2, 3, and 4, the values of OPD_{ave} fall about 6.6%, 4.8%, and 2.9%, respectively, and the values of OPD_{rms} fall about 66.7%, 62.5%, and 0.5%, respectively. The wavefront distortions are similar to those of beam 2. This indicates that the flow features that affect the beam emitted at the same viewing angle are very similar.

Figure 12 clearly shows the significant influence of the dominant flow features and large-scale structures on the wavefront distortions of all six beams. To study the OPD_{Norm} distributions of different density fields, the OPD_{Norm} values of beams 1 and 5 at 1.397 ms are given in Figs. 13 and 14, respectively. The OPD_{Norm} distributions of beams 1 and 5 transmitted through the initial field can be found in Fig. 7. According to the OPD_{Norm} shown in Fig. 13(c), when higher-order modes are removed from the flow field, the distribution of OPD_{Norm} does not seem to change, which explains the small influence of small-scale structures on the wavefront distortion. When the features in modes 3 to 32 are removed, the OPD_{Norm} shown in Fig. 13(b) is greatly reduced, but the distribution is still asymmetric because the wake lateral shift components shown in modes 1 and 2 are included in the flow field and lead to the asymmetric distribution of the refractive index in the beam path. When all of the dominant flow features shown in the

first 20 modes are removed, the OPD_{Norm} shown in Fig. 13(a) is significantly reduced, and the distribution becomes more symmetrical. The OPD_{Norm} distributions of beam 5 presented in Fig. 14 show the same regularity as those of beam 1. With the removal of the higher-order modes, the OPD_{Norm} is almost unchanged. With the removal of modes 3 to 32, the OPD_{Norm} is considerably reduced, but the distribution is still asymmetrical. With the removal of all of the lower-order modes from 1 to 20, the OPD_{Norm} falls significantly, and the distribution is quite symmetrical.

4. CONCLUSION

In this study, the flow field of a transonic flow over a hemispherical turret is simulated using the IDDES method with a modified sub-grid scale to provide a basic understanding of flow control and reduce wavefront distortion. The OPL is calculated using a third-order Runge–Kutta ray-tracing method. The POD method is implemented to study the dominant features of the flow field, and some relevant POD modes are removed to study the effects of different flow features on wavefront distortion.

For the transonic flow field, OPD_{ave} and OPD_{rms} increase along with an increase in the viewing angle. However, they increase quite slowly when the beam is transmitted through the shock region or closer to the shock region. The Fourier series expansion amplitude of $OPD_{rms,s}$ is relatively large at about $St=0.35$.

In the first two POD modes, the lateral wake shift, fluctuating at about $St=0.15$, contributes the most energy to the flow field. Modes 3 and 4 present a wake fluctuation in the wall-normal direction at about $St=0.35$. These two features are dominant and the most important for transonic flow over a turret. Moreover, the components of both dominant features are also found in certain higher-order modes.

Three density fields are reconstructed with different modes containing 30% of the mode energy removed. The wavefronts are slightly distorted when the beams are transmitted through field 2, which removes modes 1 to 20. The wavefront distortions of the beams that are transmitted through field 3, which removes modes 3 to 32, are also greatly reduced, particularly the amplitudes at $St=0.35$. However, due to the existence of the features in modes 1 and 2, the amplitude at St below 0.2 is still very large. The lateral shift of the wake leads to the asymmetry of OPD distribution. When the higher-order modes from 21 to 92 are removed, the wavefront distortions of all of the beams are slightly reduced. The wavefront distortion of the beams transmitted through the transonic flow field is mainly affected by the dominant flow features and large-scale structures. This work suggests that passive flow control has potential applications, as it induces an additional shear layer or generates additional smaller-scale structures to adjust the initial flow. Further study of the effects of different flow features on different wavefront components needs to be

performed to identify the capability of passive flow control, considering adaptive optical systems.

ACKNOWLEDGEMENTS

This work was supported by the National Natural Science Foundation of China (Grant No. 11972304 & 12272312) and Aeronautical Science Foundation of China (Grant No. 2019ZA053005).

REFERENCES

- Anson, M. and L. Zhang (1995). On-site graphics for planning and communicating the use of site space. In Y. Loo (Ed.), *Proceedings of the Fifth East Asia-Pacific Conference on Structural Engineering and Construction*, Gold Coast, Australia, 883-888. Griffith University.
- Beresh, S. J., J. F. Henfling, R. W. Spillers and B. O. Pruett (2016). Unsteady shock motion in a transonic flow over a wall-mounted hemisphere. *AIAA Journal* 54(11), 3509-3515.
- Bhattacharya, S. and A. Ahmed (2020). Effect of aspect ratio on the flow over a wall-mounted hemispherical turret. *International Journal of Heat and Fluid Flow* 84, 108600.
- Bhattacharya, S. and J. W. Gregory (2015a). Effect of three-dimensional plasma actuation on the wake of a circular cylinder. *AIAA Journal* 53(4), 958-967.
- Bhattacharya, S. and J. W. Gregory (2015b). Investigation of the cylinder wake under spanwise periodic forcing with a segmented plasma actuator. *Physics of Fluids* 27(1), 014102.
- Bhattacharya, S. and J. W. Gregory (2018). Optimum-wavelength forcing of a bluff body wake. *Physics of Fluids* 30(1), 015101.
- Bhattacharya, S. and J. W. Gregory (2020). The effect of spatially and temporally modulated plasma actuation on cylinder wake. *AIAA Journal* 58(9), 3808-3818.
- Born, M. and E. Wolf (2013). *Principles of optics: electromagnetic theory of propagation, interference and diffraction of light*. Elsevier.
- Coirier, W. J., M. Whiteley, D. J. Goorskey, R. Drye, J. Barber, J. Stutts and C. Porter (2014). Aero-optical evaluation of notional turrets in subsonic, transonic and supersonic regimes. In *45th AIAA Plasmadynamics and Lasers Conference*, Atlanta, GA.
- De Lucca, N. G., S. V. Gordeyev and E. J. Jumper (2013). In-flight aero-optics of turrets. *Optical Engineering* 52(7), 071405.
- De Lucca, N. G., S. Gordeyev, J. J. Morrida, E. J. Jumper and D. J. Wittich (2018). Modal analysis of the surface pressure field around a hemispherical turret using pressure sensitive paint. In *2018 AIAA Aerospace Sciences Meeting*, Kissimmee, Florida.

- Gilbert, K. G. and L. J. Otten (1982). *Aero-optical phenomena*. American Institute of Aeronautics and Astronautics.
- Wolfe, W. L. and Zissis, G. J. (Eds) (1978). *The Infrared Handbook*. Washington, DC: Office of Naval Research.
- Gordeyev, S., J. Cress, A. Smith and E. Jumper (2010). Improvement in optical environment over turrets with flat window using passive flow control. In *41st Plasmadynamics and Lasers Conference*, Chicago, Illinois.
- Gordeyev, S. and E. Jumper (2010). Fluid dynamics and aero-optics of turrets. *Progress in Aerospace Sciences* 46(8), 388-400.
- Gordeyev, S., A. Vorobiev, E. J. Jumper, S. P. Gogineni and D. J. Wittich (2016). Studies of flow topology around hemisphere at transonic speeds using time-resolved oil flow visualization. In *54th AIAA Aerospace Sciences Meeting*, San Diego, California, USA.
- Guseva, E. K., A. V. Garbaruk and M. K. Strelets (2017). Assessment of delayed DES and improved delayed DES combined with a shear-layer-adapted subgrid length-scale in separated flows. *Flow, Turbulence and Combustion* 98(2), 481-502.
- Jeong, J. and F. Hussain (1995). On the identification of a vortex. *Journal of Fluid Mechanics* 285, 69-94.
- Joshi, K. and S. Bhattacharya (2019). Large-eddy simulation of the effect of distributed plasma forcing on the wake of a circular cylinder. *Computers & Fluids* 193, 104295.
- Jumper, E. J., M. Zenk, S. Gordeyev, D. Cavalieri and M. R. Whiteley (2012). The airborne aero-optics laboratory, AAOL. In *Acquisition, Tracking, Pointing, and Laser Systems Technologies XXVI*. International Society for Optics and Photonics.
- Jumper, E. J., M. A. Zenk, S. V. Gordeyev, D. A. Cavalieri and M. Whiteley (2013). Airborne aero-optics laboratory. *Optical Engineering* 52(7), 071408.
- Jumper, E. J., S. Gordeyev, D. Cavalieri, P. Rollins, M. Whiteley and M. Krizo (2015). Airborne aero-optics laboratory-transonic (aaol-t). In *53rd AIAA Aerospace Sciences Meeting*, Kissimmee, Florida.
- Jumper, E. J. (2018). *Airborne Aero-Optical Laboratory-Transonic*. Notre Dame Univ In Notre Dame.
- Kamel, M. S., K. Wang and M. Wang (2019). Numerical prediction of aero-optical distortions by transonic flow over a cylindrical turret. In *AIAA Scitech 2019 Forum*, San Diego, California.
- Liu, Z., Y. Yang, W. Zhou and A. Gong (2014). Study of unsteady separation flow around airfoil at high angle of attack using hybrid rans-les method. *Acta Aeronautica et Astronautica Sinica* 35(2), 372-380.
- Mani, A., P. Moin and M. Wang (2009). Computational study of optical distortions by separated shear layers and turbulent wakes. *Journal of Fluid Mechanics* 625, 273-298.
- Menter, F. R. (1994). Two-equation eddy-viscosity turbulence models for engineering applications. *AIAA journal* 32(8), 1598-1605.
- Menter, F. R. and M. Kuntz (2004). Adaptation of eddy-viscosity turbulence models to unsteady separated flow behind vehicles. In *The aerodynamics of heavy vehicles: trucks, buses, and trains*. Berlin, Heidelberg.
- Morrida, J. J., S. Gordeyev, E. J. Jumper, S. P. Gogineni, A. Marruffo and D. J. Wittich (2016). Investigation of shock dynamics on a hemisphere using pressure and optical measurements. In *54th AIAA Aerospace Sciences Meeting*, San Diego, California, USA.
- Porter, C., S. Gordeyev, M. Zenk and E. Jumper (2013). Flight measurements of the aero-optical environment around a flat-windowed turret. *AIAA journal* 51(6), 1394-1403.
- Shur, M. L., P. R. Spalart, M. K. Strelets and A. K. Travin (2008). A hybrid RANS-LES approach with delayed-DES and wall-modelled LES capabilities. *International Journal of Heat and Fluid Flow* 29(6), 1638-1649.
- Shur, M. L., P. R. Spalart, M. K. Strelets and A. K. Travin (2015). An enhanced version of DES with rapid transition from RANS to LES in separated flows. *Flow, Turbulence and Combustion* 95(4), 709-737.
- Spalart, P. R., W. H. Jou, M. Strelets and S. R. Allmaras (1997). Comments on the feasibility of LES for winds, and on a hybrid RANS/LES approach. *Advances in DNS/LES: Direct Numerical Simulation and Large Eddy Simulation* 137-148.
- Spalart, P. R. (2000). Strategies for turbulence modelling and simulations. *International Journal of Heat and Fluid Flow* 21(3), 252-263.
- Spalart, P. R., S. Deck, M. L. Shur, K. D. Squires, M. K. Strelets and A. Travin (2006). A new version of detached-eddy simulation, resistant to ambiguous grid densities. *Theoretical and Computational Fluid Dynamics* 20(3), 181-195.
- Strelets, M. (2001). Detached eddy simulation of massively separated flows. In *39th Aerospace sciences meeting and exhibit*, Reno, NV, USA.
- Szydlowski, J. and M. Costes (2004). Simulation of flow around a static and oscillating in pitch NACA 0015 airfoil using URANS and DES. In *Heat Transfer Summer Conference*, Charlotte, North Carolina, USA.
- Taira, K., S. L. Brunton, S. T. Dawson, C. W. Rowley, T. Colonius, B. J. McKeon and L. S. Ukeiley (2017). Modal analysis of fluid flows:

S. Tang *et al.* /*JAFM*, Vol. 16, No. 3, pp. 443-458, 2023.

- An overview. *Aiaa Journal* 55(12), 4013-4041.
- Tian, R. Z., H. Y. Xu, Q. L. Dong and Z. Y. Ye (2020). Numerical investigation of aero-optical effects of flow past a flat-windowed cylindrical turret. *Physics of Fluids* 32(5), 056103.
- Vorobiev, A., S. Gordeyev, E. J. Jumper, S. Gogineni, A. Marruffo and D. J. Wittich (2014). A Low-Dimensional Model of Shock-Wake Interaction Over Turrets at Transonic Speeds. In *45th AIAA Plasmadynamics and Lasers Conference*, Atlanta, GA.
- Wang, K., M. Wang, S. Gordeyev and E. Jumper (2010). Computation of aero-optical distortions over a cylindrical turret with passive flow control. In *41st Plasmadynamics and Lasers Conference*, Chicago, Illinois.
- Wang, M., A. Mani and S. Gordeyev (2012). Physics and computation of aero-optics. *Annual Review of Fluid Mechanics* 44, 299-321.
- Weston, D. and S. E. Sherer (2019). Comparison of Computational and Experimental Results on a Transonic Hemisphere. In *AIAA Scitech 2019 Forum*, San Diego, California.